

Systematic bias due to mismodelling precessing binary black hole ringdown

Cheng Foo^{1,2} and Eleanor Hamilton^{3,4}

¹*Max Planck Institute for Gravitational Physics (Albert Einstein Institute), D-14476 Potsdam, Germany*

²*Institute for Theoretical Physics, ETH Zürich, Wolfgang-Pauli-Str. 27, 8093 Zürich, Switzerland*

³*Departament de Física, Universitat de les Illes Balears,*

IAC3 - IEEC, Crta. Valldemossa km 7.5, E-07122 Palma, Spain

⁴*Physik-Institut, Universität Zürich, Winterthurerstrasse 190, 8057 Zürich, Switzerland*

(Dated: August 6, 2024)

Accurate waveform modelling is crucial for parameter estimation in gravitational wave astronomy, impacting our understanding of source properties and the testing of general relativity. The precession of orbital and spin angular momenta in binary black hole (BBH) systems with misaligned spins presents a complex challenge for gravitational waveform modelling. Current precessing BBH waveform models employ a co-precessing frame, which precesses along with the binary. In this paper, we investigate a source of bias stemming from the mismodelling of ringdown frequency in the co-precessing frame. We find that this mismodelling of the co-precessing frame ringdown frequency introduces systematic biases in parameter estimation, for high mass systems in particular, and in the Inspiral-Merger-Ringdown (IMR)-consistency test of general relativity. Employing the waveform model IMRPHENOMXPHM, we conduct an IMR-consistency test using a Fisher matrix analysis across parameter space, as well as full injected signal parameter estimation studies. Our results show that this mismodelling particularly affects BBH systems with high mass ratios, high spin magnitudes, and highly inclined spins. These findings suggest inconsistencies for all waveform models which do not address this issue.

I. INTRODUCTION

Since the first detection of gravitational waves (GWs) in 2015, 90 GW events have been observed by the LIGO-Virgo-KAGRA Collaboration (LVK), primarily originating from binary black hole (BBH) systems [1–4]. These systems, composed of two black holes orbiting around each other, emit GWs as they lose orbital energy, gradually spiralling towards each other before merging into a single, perturbed black hole. GWs contain information of the astrophysical systems that produced them, such as the masses and spins of the black holes, and can also be used to test our physical theory of general relativity (GR).

Parameter estimation, a process to extract properties of the source from GWs, relies on comparing accurate theoretical waveforms with GW data. Systematic errors in theoretical waveforms can introduce biases in parameter estimation [5–7]. The increasing sensitivity of current detectors, in particular the LIGO, Virgo and KAGRA detectors [8–11], and the construction of next generation detectors such as Cosmic Explorer [12, 13], Einstein Telescope [14] and LISA [15], underscore the need for more precise waveform models. Current BBH waveform models used by the LVK can be split into three families, the phenomenological models “PHENOM” [16–29], the effective-one-body models “SEOBNR” [30–37], and the numerical relativity surrogate models “NRSURROGATE” [38–46].

GW signals from BBHs on quasi-circular orbits are characterised by the masses and spins of the binary. Modelling efforts are complicated by eccentricity and spin effects. In this paper, we are particularly interested in the effects of black hole spins with components in the orbital

plane of the binary. The orientation of spins in generic BBH systems can vary widely, depending on their formation process [47, 48]. When the spins of the two black holes in a binary are misaligned with the orbital angular momentum, both the orbital and spin angular momenta will precess about the total orbital angular momentum, a phenomenon known as (spin) precession [49–51]. This results in intricate modulations of both the amplitude and phase of the GW signal, which are difficult to model [52, 53]. Waveform models for precessing BBHs usually employ a co-precessing frame, which precesses along with the binary. In this frame the waveform is well approximated by an aligned-spin waveform with a modified final spin [54]. In current models, this co-precessing frame is either defined by the orbital dynamics [23, 35, 37], or by the optimal emission direction [27, 29], which is the direction in which majority of the power is emitted. Current “NRSURROGATE” models instead use a co-orbital frame, which not only tracks the precession of the system using waveform quantities but also the instantaneous orbital phase, and interpolates numerical relativity waveforms in this frame [42].

In order to obtain the inertial frame waveform, a time- or frequency-dependent rotation is applied to the co-precessing waveform, e.g. see Refs. [25–27, 37, 50, 51]. This procedure is called ‘twisting-up’, and is performed with three time-/frequency-dependent Euler angles $\{\alpha, \beta, \gamma\}$. Typically, these angles are chosen to describe the orientation of the co-precessing frame z direction with respect to the total angular momentum \mathbf{J} .

In this paper, we investigate a source of systematic bias in precessing BBH waveforms affecting the ringdown section of the waveform. Ringdown is the final stage of a GW signal from a BBH system, where the system can be

modeled as a single perturbed black hole emitting GWs. These GWs are characterised by a set of complex frequencies, called quasinormal modes (QNMs), where the real parts are the ringdown frequencies [55, 56]. Several works have shown complicated phenomenology in the ringdown for precessing BBH systems [57–59], which if mismodelled could lead to systematic bias in parameter estimation. The source of bias investigated here is due to employing the ringdown frequency derived from perturbation theory directly in the co-precessing frame, while the results from perturbation theory are only valid in the inertial \mathbf{J} -frame [27, 58]. This mismodelling of co-precessing frame ringdown frequencies is present in many precessing models, such as IMRPHENOMXPHM [23], and SEOBNRv4PHM [35]. In this paper we will study IMRPHENOMXPHM, one of the key models employed by the LVK in the analysis of detected GW signals.

Understanding this source of systematic bias is relevant for both the data analysis of high mass precessing BBH systems, as well as for tests of GR which rely on the ringdown [5]. Several proposed tests of GR using GWs exist, and one such test is the Inspiral-Merger-Ringdown (IMR)-consistency test [60, 61]. The IMR-consistency test is based on GW data from a BBH merger. The fundamental concept underlying this test is that the mass and spin of the remnant black hole determined using two different segments of the GW signal, the inspiral (low-frequency) section and the ringdown (high-frequency) section, should be consistent [62]. Assuming accurate parameter estimation, lack of consistency indicates a potential GR violation.

Our analysis shows that mismodelling the co-precessing frame ringdown frequency leads to inaccuracies in GW data analysis. This is particularly so in highly precessing parameter space regions, especially at high values of mass ratio q , spin magnitude χ and spin misalignment with orbital angular momentum $\theta \sim 150^\circ$. This will most strongly impact GW data analysis in two situations: first, when running parameter estimation on full signals from heavy mass systems, where the signal is dominated by the merger-ringdown; and second, when performing an IMR-consistency test. Our analysis shows one example of how mismodelling in the merger-ringdown portion of the signal can negatively impact parameter estimation and tests of GR.

We will first consider the impact of this source of systematic bias using Fisher analysis. This enables us to study the effect of this source of bias in isolation. We can therefore consider the impact not only on our ability to correctly measure the properties of the source from the GW signal, but also the consequent effect of these uncertainties on downstream analyses – in particular tests of GR. We will then consider a complete parameter estimation analysis. This will give a more realistic picture of the impact on GW data analysis. However, this analysis is less controlled and does not permit the investigation of a single source of waveform systematics. We therefore consider only the effect on parameter estimation and leave

considerations of tests of GR to future, improved models.

The structure of this work is as follows. In Sec. II A, we introduce the source of systematic bias under investigation in more detail. We then introduce the IMR-consistency test and the Fisher matrix formalism in Sec. II B and Sec. II C, as these are the main tools for our analysis. In Sec. III, we discuss the methodology of our analysis, before presenting results across parameter space. Finally, in Sec. IV, we perform signal injections and recovery using Bayesian analysis, to determine the effect of this bias on real parameter estimation.

II. PRELIMINARIES

In general, a quasi-circular BBH system composed of two black holes with masses m_1 and m_2 can be described by 8 intrinsic parameters. These are the mass ratio of the binary $q = m_1/m_2$, the total mass of the system $M = m_1 + m_2$, and two black hole spins \mathbf{S}_1 and \mathbf{S}_2 . We use the dimensionless black hole spins $\boldsymbol{\chi}_1$ and $\boldsymbol{\chi}_2$, where $\boldsymbol{\chi}_i = \mathbf{S}_i/m_i^2$. The spins can be decomposed into their components parallel and perpendicular to the direction of the Newtonian orbital angular momentum $\hat{\mathbf{L}}$, given by $\chi_i^\parallel = \boldsymbol{\chi}_i \cdot \hat{\mathbf{L}}$ and $\chi_i^\perp = \chi_i - \chi_i^\parallel \hat{\mathbf{L}}$ respectively.

Dominant effects due to the spins of the black holes can be described by a combination of the spin components to two effective parameters $(\chi_{\text{eff}}, \chi_p)$. χ_{eff} describes dominant aligned-spin effects, and is given by [63, 64]

$$\chi_{\text{eff}} = \frac{m_1 \chi_1^\parallel + m_2 \chi_2^\parallel}{m_1 + m_2}. \quad (1)$$

On the other hand, χ_p describes dominant precession effects, parameterising spin perpendicular to the orbital angular momentum, and is given by

$$\chi_p = \frac{S_p}{m_1^2}, \quad (2)$$

where $S_p = \frac{1}{A_1} \max(A_1 S_1^\perp, A_2 S_2^\perp)$, $A_1 = 2 + 3m_2/(2m_1)$, and $A_2 = 2 + 3m_1/(2m_2)$ [65].

Since dominant spin effects are given by these two effective parameters, we can thus use a single-spin mapping to describe a two-spin system, which will give us the same phenomenology to leading order [27]. We will need signals of signal-to-noise ratios (SNRs) of 100 or more to make individual spin measurements, so we neglect two-spin effects for now [21]. For the rest of this paper, we consider only single-spin systems, where the more massive black hole has a spin, and the less massive black hole does not. In addition, we choose the convention where $m_1 \geq m_2$, and thus $q \geq 1$. The single spin on the larger black hole is described by two parameters, its magnitude χ , and the angle it makes with \mathbf{L} , θ . The parameter space we work with is thus (q, χ, θ) .

A. Modelling ringdown in precessing BBH systems

GWs are often decomposed into harmonics, which provide a useful basis for modelling the radiation pattern. However, the choice of harmonics depends on the nature of the source. GWs produced by the inspiral phase of a binary system are more conveniently modelled using spherical harmonics, while GWs produced by a black hole ‘ringing down’ are best decomposed into spheroidal harmonics [19, 24, 58, 66]. It is common practice to decompose the full IMR signal into spherical harmonics [19, 67].

QNMs comprising the ringdown signal are uniquely determined by the mass and spin of the final black hole. The spin s -weighted QNM frequencies ω_{lmn} , associated with projections onto spheroidal harmonics, are characterised by their angular number l and azimuthal angle m . We consider only contributions from the fundamental QNMs ($n = 0$) [58]. For the rest of this paper the imaginary part $\text{Im}(\omega_{lm})$ is not relevant to us. When we refer to ω_{lm} from here onward, we are referring only to the real part $\text{Re}(\omega_{lm})$. In addition, we make the assumption that for the dominant $(2, |2|)$ multipole in the co-precessing frame, we can use the spheroidal characteristic QNM frequency to characterise the frequency in the spherical harmonic basis.

As discussed in the Introduction, precessing waveform models employ a co-precessing frame model, which is then twisted up to an inertial frame waveform model using the Euler angles (α, β, γ) . The angle β is related to the opening angle of the precession cone during the inspiral [53, 68]. During the ringdown, β is given by the orientation of the final spin relative to the optimal emission direction postmerger [58]. For further discussion on QNMs, see [66], and for further discussion on the direction of emission for GWs from a perturbed black hole, see Sec. IX.B of [27].

The rotation from the co-precessing frame to the inertial frame will introduce a shift in GW frequency, and since a rotation is still applied to the ringdown section of the waveform model, this means a shift in ringdown frequency [27]. The shift in ringdown frequency from its co-precessing frame value ω_{lm}^{CP} to its inertial frame value ω_{lm}^{J} was derived in Ref. [58], and is given by

$$\omega_{lm}^{\text{J}} = \omega_{lm}^{\text{CP}} + m(1 - |\cos \beta_f|)\dot{\alpha}, \quad (3)$$

where m is the QNM azimuthal number, $\dot{\alpha}$ is the time derivative of the Euler angle α , and β_f is the final ringdown value β settles into after merger.

If the inertial frame ringdown frequency is applied in the co-precessing frame model, it will then be shifted away from the correct value when the model is twisted up to the inertial frame. The final model in the inertial frame will then have the wrong ringdown frequency. This is the case in some current and historical models, e.g. [23, 35], and has been corrected in more recent models [27, 29, 37]. In the rest of this paper, we investigate how this source of bias will affect data analysis using IMRPHENOMXPHM.

In the construction of the merger-ringdown section of IMRPHENOMXPHM, the final mass and spin of the remnant (M_f, χ_f) are calculated using fits to numerical relativity (NR) and a correction to the final spin due to precessional effects [23]. The associated QNMs for these remnant parameters are then incorrectly employed in constructing the co-precessing frame ringdown waveform. As described above with Eq. (3), the final ω_{lm} value (once rotated back to the inertial frame) will thus be wrong, having been shifted away from its true value. This inappropriate choice of co-precessing frame QNM frequency introduces systematic bias in the merger-ringdown section of the waveform model, which could lead to inaccurate parameter estimation results. In particular, data analysis of high mass precessing BBH systems will be affected, since more of the ringdown section of the signal will be in the LVK sensitivity band.

It is important to understand where in parameter space these effects are most prominent, as we should be cautious with parameter estimation results in these regions. Tests of GR, including the IMR-consistency test, will also be affected. We anticipate this to be extreme regions of parameter space, with high values of q and χ , where precessional effects are more pronounced. Naively, we might expect that the effects of precession are maximised when the initial binary spins are fully in-plane, which would correspond to $\theta = 90^\circ$. However, this systematic bias is actually maximised at $\theta \approx 150^\circ$. This corresponds roughly to where $\cos(\beta_f) \approx 0$, as can be seen from Fig. 6 and the surrounding discussion in Ref. [58]. This would maximise the shift away from the true QNM ringdown frequency in Eq. (3).

Physically, this can be understood as follows. Ref. [27] found, using NR data, that β collapses through merger, rapidly dropping to a lower value. During inspiral, the precession cone (as measured by β) will be largest for large in-plane spins, where $\theta \sim 90^\circ$. For systems with higher mass ratios and close to anti-aligned-spins, β can take values greater than 90° , although the precession cone is bounded by 90° due to symmetry about the orbital plane. For these systems, as β collapses it moves closer to a value of 90° , and the precession cone actually increases, meaning that precession effects are maximal for these systems during merger and ringdown. Thus, the optimal emission direction, which corresponds to the direction of the perturbation of the remnant [58], will be close to orthogonal with final spin. The effect will thus be most pronounced for high values of θ , excluding $\theta \approx 180^\circ$, which will just stay close to anti-aligned with the final spin.

B. IMR-Consistency Test

Various tests of GR using GWs have been proposed [69]. One such test is the IMR-consistency test [60, 61], which checks for consistency between two sections of the GW signal.

For the inspiral, which is the low-frequency part of the signal, initial masses and spins are first estimated using parameter estimation. These are then converted to remnant parameters using NR fits. The remnant parameters can also be similarly inferred from the post-merger, high-frequency part of the signal. These two sets of parameters are then compared. Assuming an accurate parameter estimation, we expect the two sets of estimates to be consistent with each other if GR is valid, and an inconsistency indicates a potential deviation from GR [60, 61].

To have sufficient SNR in each of the sections of the waveform, the full signal is used, split into two at an appropriate cutoff frequency. This is in contrast to the original idea, which was to use part of the signal from the early inspiral, and part of the signal from the ringdown. The frequency typically chosen is f_{ISCO} [60], which corresponds to twice the orbital frequency of a test particle orbiting at the innermost stable circular orbit of the remnant black hole formed by the system [60, 61, 70]. The frequency f_{ISCO} is not exactly the point where the inspiral regime moves to the merger regime, but it is a reasonable choice [60, 71].

The mismodelling of the co-precessing ringdown frequency discussed in Sec. II A means that the ringdown waveform is inconsistent with the inspiral waveform. If such a model is used for an IMR-consistency test on precessing systems, this bias will lead to inconsistencies that are unphysical. To analyse this issue across parameter space, we assess the consistency of the inspiral and ringdown portions of the IMRPHENOMXPHM model by extracting properties directly from the waveforms. We determine whether the two estimates agree to within a given number of standard deviations. To calculate this error, we use the Fisher-matrix formalism.

C. Fisher matrix formalism

When a GW passes through a detector, the recorded data $s(t)$ is

$$s(t) = h(t) + n(t), \quad (4)$$

where $h(t)$ is the GW strain, and $n(t)$ is the noise present during the detection. For the Fisher-matrix formalism, we assume that the noise is Gaussian and stationary [72]. In data analysis, we look for the collection of parameters that characterise the GW signal $\theta = \{\theta_1, \dots, \theta_N\}$. For a true signal $h(t; \theta_{tr})$ inside GW data, described by real parameters θ_{tr} , consider parameters θ_{tr}^i within the parameter set θ_{tr} . Our estimates for θ_{tr}^i are given by maximum likelihood estimators $\hat{\theta}_{ML}^i$, and we can then express θ_{tr}^i as $\theta_{tr}^i = \hat{\theta}_{ML}^i + \Delta\theta^i$, where $\Delta\theta^i$ represents the errors for each of these parameters [73].

The Fisher matrix is given by

$$\Gamma_{ij} = \left(\frac{\partial h}{\partial \theta^i} \middle| \frac{\partial h}{\partial \theta^j} \right), \quad (5)$$

evaluated at $\theta = \hat{\theta}_{ML}$. This object Γ_{ij} is known as the *Fisher information matrix* [74]. It can be interpreted as the inverse of the covariance Σ for our posterior probability distribution $p(\theta_{tr}|s)$ [72],

$$\langle \Delta\theta^i \Delta\theta^j \rangle = (\Gamma^{-1})^{ij} = \Sigma^{ij}. \quad (6)$$

In essence, the Fisher information matrix quantifies the precision of our parameter estimation, and allows us to calculate the 1σ statistical errors in parameters θ_{tr}^i . This 1σ value is simply given by the square root of the diagonal elements of the covariance matrix:

$$\sigma^i = \sqrt{\Sigma^{ii}} = \sqrt{(\Gamma^{-1})^{ii}} \quad (7)$$

The use of this formalism can thus provide us with a covariance matrix, assuming high SNR and stationary, Gaussian noise [72].

For our specific analysis in Sec. III, we will analyse a system with a three-dimensional parameter space described by (q, χ, θ) . The relevant Fisher matrix for such a system can be written as follows:

$$\Gamma^{(3)} = \begin{pmatrix} \Gamma_{qq} & \Gamma_{q\chi} & \Gamma_{q\theta} \\ \Gamma_{\chi q} & \Gamma_{\chi\chi} & \Gamma_{\chi\theta} \\ \Gamma_{\theta q} & \Gamma_{\theta\chi} & \Gamma_{\theta\theta} \end{pmatrix} \quad (8)$$

We need derivatives of the waveform to calculate each of these components, as in Eq. (5), and we solve for these numerically.

The covariance matrix for our inspiral three parameter system is $(\Gamma^{(3)})^{-1} = \Sigma^{(3)}$. For our analysis, we will need to convert this into the covariance matrix for our remnant parameters,

$$\tilde{\Sigma} = \begin{pmatrix} \tilde{\Sigma}_{M_f M_f} & \tilde{\Sigma}_{M_f \chi_f} \\ \tilde{\Sigma}_{\chi_f M_f} & \tilde{\Sigma}_{\chi_f \chi_f} \end{pmatrix}. \quad (9)$$

Following the method set out in Ref. [75], the elements of the matrix above can be calculated as follows:

$$\tilde{\Sigma}_{M_f M_f} = \delta M_f^2 = \sum_{i,j} \left(\frac{\partial M_f}{\partial \theta^i} \right) \left(\frac{\partial M_f}{\partial \theta^j} \right) \Sigma_{ij}^{(3)}, \quad (10)$$

$$\tilde{\Sigma}_{\chi_f \chi_f} = \delta \chi_f^2 = \sum_{i,j} \left(\frac{\partial \chi_f}{\partial \theta^i} \right) \left(\frac{\partial \chi_f}{\partial \theta^j} \right) \Sigma_{ij}^{(3)}, \quad (11)$$

$$\tilde{\Sigma}_{M_f \chi_f} = \tilde{\Sigma}_{\chi_f M_f} = \sum_{i,j} \left(\frac{\partial M_f}{\partial \theta^i} \right) \left(\frac{\partial \chi_f}{\partial \theta^j} \right) \Sigma_{ij}^{(3)}. \quad (12)$$

The covariance matrix can be represented as an error ellipse in plots. To plot our error ellipses in the $M_f - \chi_f$ plane, we need the semi-major axis a , the semi-minor axis b , and the angle θ_{ellipse} , which is the counter-clockwise angle relative to the horizontal axis M_f . In order to obtain a and b , we need to calculate the eigenvalues of our covariance matrix, Λ_{\pm} . For a 1σ error ellipse, the semi-major axis a and the semi-minor axis b are related to the eigenvalues as follows [75]:

$$a = \sqrt{\Lambda_+} \quad b = \sqrt{\Lambda_-}. \quad (13)$$

The angle θ_{ellipse} can be calculated from the final parameter covariance matrix [75],

$$\theta_{\text{ellipse}} \approx -\frac{1}{2} \arctan \left(\frac{2\tilde{\Sigma}_{M_f\chi_f}}{\tilde{\Sigma}_{M_f M_f} \tilde{\Sigma}_{\chi_f \chi_f}} \right). \quad (14)$$

III. IMR-CONSISTENCY TEST STUDY

In this Section, we conduct an ‘IMR-consistency test’ on waveforms generated by the IMRPHENOMXPHM model. Our goal here is to investigate the source of systematic bias described in Sec. II A, and to determine the region of parameter space where it will affect data analysis.

We begin by generating a waveform instance for a given binary configuration with specific input inspiral parameters using PyCBC [76]. We then split the waveform instance into two sections at an appropriate cutoff frequency, which we choose to be f_{ISCO} [77, 78]. For each of our two sections of the waveform, we employ distinct methods to estimate the parameters of the remnant black hole (M_f, χ_f), followed by calculating the error ellipses using the Fisher matrix formalism. We choose to employ the Fisher matrix formalism as we want to conduct our analysis across parameter space, and thus need a computationally efficient method.

If the ellipses for a particular confidence interval do not overlap, it indicates that the final parameters estimated from the two sections of our waveform are incompatible with each other up to that confidence level. In accordance with the IMR-consistency test criteria, this result implies a ‘violation of GR’. Since the model is intended to faithfully represent a GW signal as predicted by GR, this violation is non-physical and comes from inaccuracies in the waveform model.

The Fisher analysis enables us to identify the regions of parameter space where model inaccuracies will lead to this erroneous conclusion, due to systematic biases. We explore the parameter space described by (q, χ, θ) . We conduct our analysis across this parameter space for waveforms with specific SNR values, and look for predicted ‘violations of GR’ at 1σ , 2σ and 3σ confidence levels.

A. Calculating Remnant Parameters

1. Inspiral

The inspiral part of the waveform is characterised by the input intrinsic parameters. We can calculate the values of (M_f, χ_f) predicted for a binary with these input parameters using fits obtained from NR simulations.

We follow the method that IMRPHENOMXPHM uses to model the final state of a precessing system given the input inspiral parameters (c.f. Section IV.D of [23]).

For inspiral parameters (q, χ, θ) , we first find the final state $(M_f^{\parallel}, \chi_f^{\parallel})$ of the corresponding aligned-spin system parameterised by $(q, \chi \cos \theta, 0)$, using the NR fits from [79]. These fits are implemented using code from package `llondon6/positive` [80]. We then employ approximations to obtain the final state of the precessing system [23].

For the final mass, several NR fit studies have shown that there is only a weak dependence on precession [81–83]. Thus, we follow IMRPHENOMXPHM and its predecessors in setting $M_f = M_f^{\parallel}$.

For the final spin, we cannot ignore precession dependence [23]. The final spin is calculated from the aligned-system final spin χ_f^{\parallel} using

$$\chi_f = \text{sgn}(\chi_f^{\parallel}) \sqrt{\left(\chi_p \frac{m_1^2}{(m_1 + m_2)^2} \right)^2 + \left(\chi_f^{\parallel} \right)^2}. \quad (15)$$

This equation is adapted from [16, 84]. For single-spin systems with the spin on the larger black hole, $\chi_p = \chi \sin \theta$ is the in-plane spin component. This equation is then equivalent to

$$\chi_f = \text{sgn}(\chi_f^{\parallel}) \sqrt{\left(\chi \sin \theta \frac{q^2}{q^2 + 2q + 1} \right)^2 + \left(\chi_f^{\parallel} \right)^2}. \quad (16)$$

We will denote these final mass and spin values calculated from the inspiral section as $(M_f^{\text{insp}}, \chi_f^{\text{insp}})$.

2. Merger-Ringdown

Now we compute the remnant parameters from the post-merger section of our waveform, which we denote $(M_f^{\text{merg}}, \chi_f^{\text{merg}})$. This computation is more complicated than the inspiral equivalent above – since the IMRPHENOMXPHM waveforms are generated with inspiral input parameters, we need to extract the parameters directly from the generated merger-ringdown waveform. As discussed above, NR studies have shown the final mass value has a weak dependence on precession. We thus take $M_f^{\text{merg}} = M_f^{\text{insp}}$ and assume that the source of bias outlined in Sec II A will affect only χ_f . This assumption allows us to estimate the final spin χ_f^{merg} from the merger-ringdown section.

To accomplish this, we analyse the QNM spectrum of the final black hole. In particular, we want to extract the characteristic ringdown frequency ω_{22} of the $(2, |2|)$ mode. Using QNM data tables [66], which list ω_{lm} values for corresponding black hole masses and spins, we can then compute χ_f .

We generally expect a characteristic dip in the phase derivative of the aligned-spin waveform at frequency f_0 . This dip frequency coincides up to a small error with the ringdown frequency of the final black hole for an aligned-spin system, ω_{22} [17, 18, 24]. Across parameter space, the behaviour of the phase derivative of the $(2, |2|)$ mode is

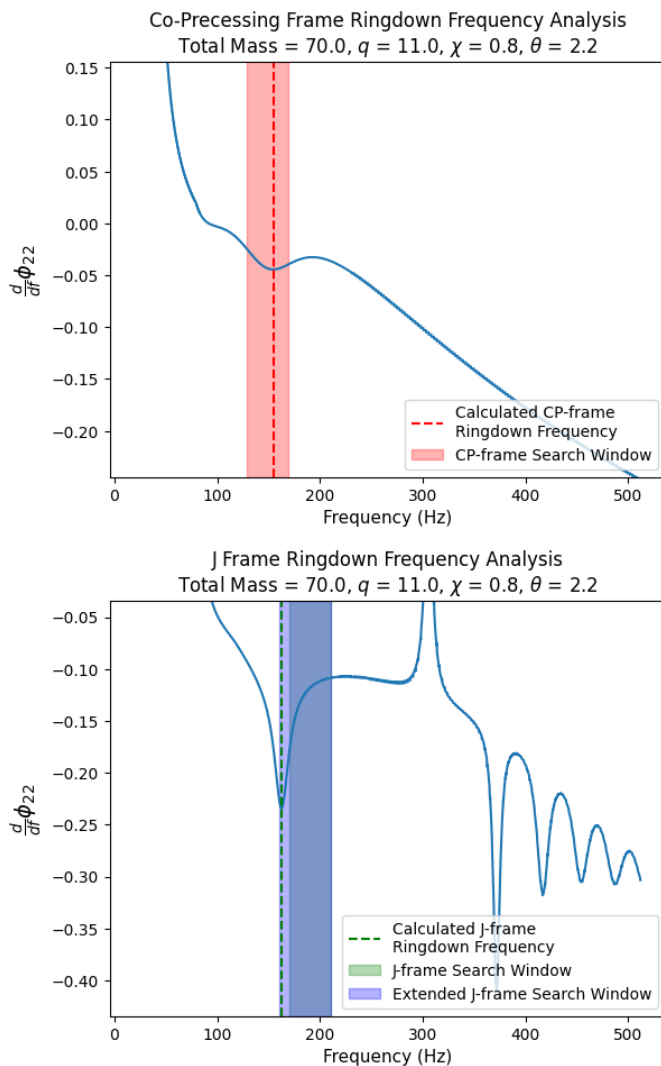


Figure 1: Two figures demonstrating our search for ω_{22} , one in the co-precessing frame (above), and one in the inertial frame (below). The dotted lines show the determined ω_{22} .

relatively well behaved for aligned-spin systems, and for precessing systems in the co-precessing frame. However, trying to search for this dip in the inertial frame phase derivative of a precessing waveform is not trivial, due to the mixing of spherical multipoles caused by the twisting up procedure [58]. As precession effects grow, the behaviour of the phase derivative is less well-behaved.

We first find an estimate of ω_{22} using the predicted remnant mass and spin values calculated in Sec. III A 1, and then computationally search for the characteristic dip in $d\phi_{22}/df$ in a window around this estimate. An example of such a search, in both the co-precessing frame and the inertial frame, can be seen in Fig. 1. Our results for ω_{22} are relatively noisy for high q , χ and θ values. In order to analyse general trends across parameter space, we generate $\omega_{22}(\theta)$ values across θ parameter space for

each $\{q, \chi\}$ used in the analysis, and perform a cubic fit through these values. The QNM frequency we use is then the value of this fit at our input θ .

To convert this QNM frequency into final spin, we create a spline from the QNM data tables [66], inputting ω_{22} and M_f^{merg} to obtain $|\chi_f^{\text{merg}}|$. We follow IMRPHENOMXPHM in setting $\text{sgn}(\chi_f) = 1$ for prograde QNM frequencies, and $\text{sgn}(\chi_f) = -1$ for retrograde QNM frequencies.

3. Final parameter difference

As a sanity check, we want to make sure that the discrepancy between χ_f^{merg} and χ_f^{insp} is entirely due to the mismodelling of the co-precessing ringdown frequency discussed in Sec. II A. To accomplish this, we need to know what the expected shift in final spin $|\Delta\chi_f^{\text{expect}}| = |\chi_f^{\text{shifted}} - \chi_f^{\text{insp}}|$ should be, where χ_f^{shifted} is the final spin after the shift of ringdown frequency away from its true value. We calculate the QNM frequency $\omega_{22}^{\text{insp}}$ associated with our inspiral remnant parameters $(M_f^{\text{insp}}, \chi_f^{\text{insp}})$, and perform the expected shift using Eq. (3), taking the Euler angles generated using the package *Cyberface/gw-phenom* [85]. These are the angles derived from an application of multiple scale analysis (MSA) [86], as utilised by IMRPHENOMXPHM. Using the shifted QNM frequency and M_f^{insp} , we then calculate χ_f^{shifted} from QNM data table splines as above [66]. Finally, we compute

$$|\Delta\chi_f^{\text{model}}| = |\chi_f^{\text{merg}} - \chi_f^{\text{insp}}|, \quad (17)$$

$$|\Delta\chi_f^{\text{expect}}| = |\chi_f^{\text{shifted}} - \chi_f^{\text{insp}}|, \quad (18)$$

across the (χ, θ) parameter space for discrete choices of q .

As can clearly be seen from Fig. 2, the similarities between the expected and actual final spin difference show that the discrepancy in final spin estimates is mainly due to the systematic bias from ω_{22} mismodelling, rather than other systematics. Note that we are not yet considering any statistical errors in our estimates of the remnant parameters – that is something we will look at next in Sec. III B.

The results here agree with our expectations that the difference in estimates will be more pronounced for extreme regions in parameter space. For $q = 4$, the two spin estimates agree generally, while for $q = 11$, there is a dramatic increase in $|\Delta\chi_f|$ at high χ, θ values. This is what we expect – as precession effects become more relevant, the shift in the ringdown frequency should increase, leading to a greater difference.

B. Computing Errors in Remnant Parameters

For each (q, χ, θ) input, we calculate the uncertainties in measurements of (M_f, χ_f) from both parts of the wave-

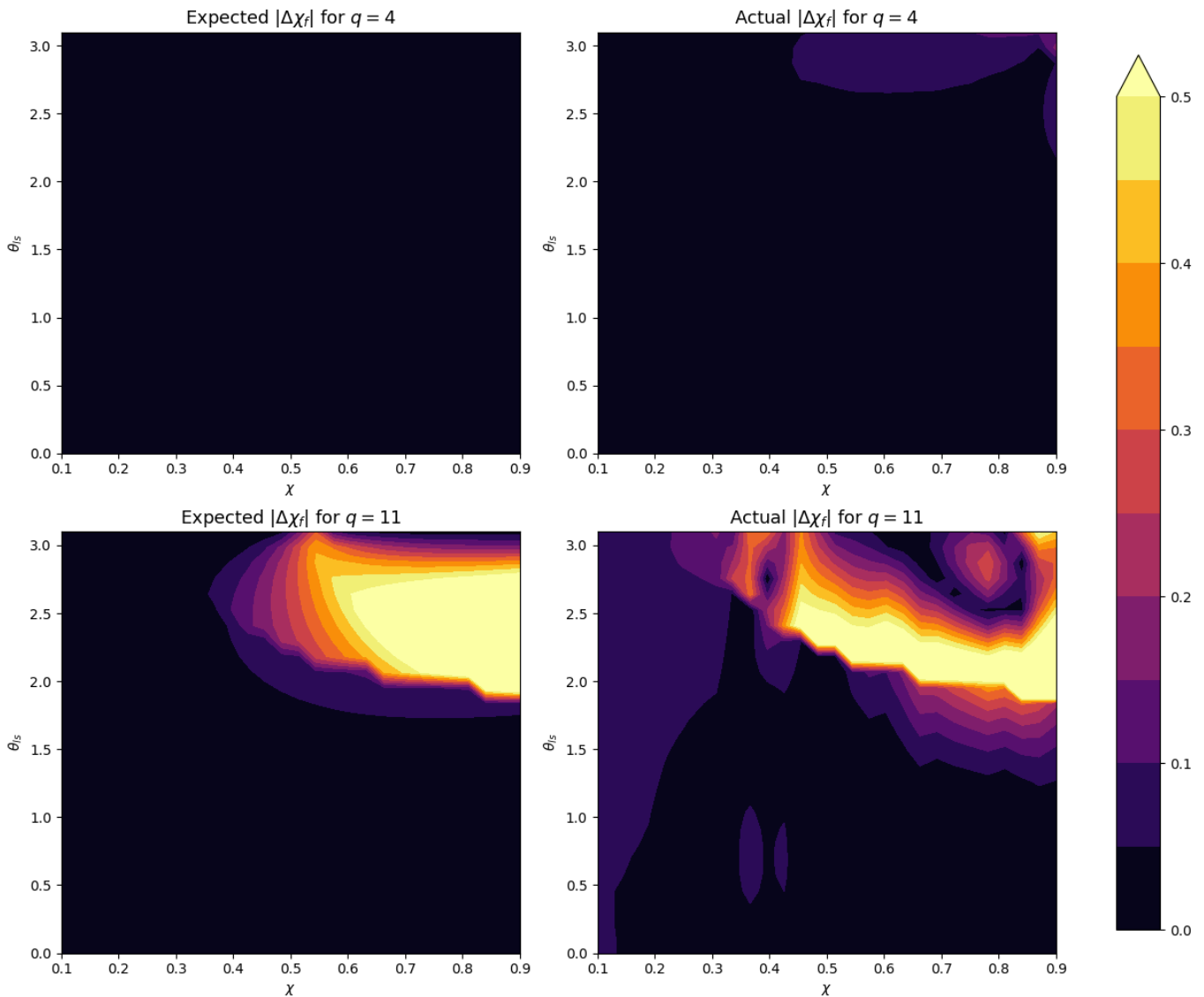


Figure 2: Figures on the left show the expected final spin difference $|\Delta\chi_f^{\text{expect}}|$ between inspiral and merger, resulting from the shift of QNM frequencies identified in Eq. (3). Figures on the right show the final spin difference $|\Delta\chi_f^{\text{model}}|$ found between inspiral and ringdown from IMRPHENOMXPHM waveforms. All systems were generated with a total mass of $70M_\odot$.

form for a signal at a given SNR. We do this using the Fisher matrix formalism detailed in Sec. II C, calculating the 3-dimensional Fisher matrix Eq. (8) for both the inspiral and for the merger-ringdown. We use numerical derivative methods to calculate the derivatives of the final parameters with respect to the input parameters. This is trivial for the inspiral, as the input parameters are simply the inspiral parameters. For the merger, this is more complicated. For example, for calculating the derivative of M_f^{merg} with respect to q , we repeat the entire analysis detailed in Section III A 2 for $q + \delta q$, and for $q - \delta q$, and perform a numerical derivative.

Having obtained the 2-dimensional covariance matrix of the remnant parameters, following the analysis in Sec.

II C to obtain Eq. (9), we can then compute the error ellipses for the final mass and spin. Putting all above results together, we perform an IMR-consistency test on the waveform model IMRPHENOMXPHM across a large region of parameter space.

C. Results of analysis across parameter space

Our findings reveal that the model incorrectly predicts violations of GR in more extreme regions of parameter space (i.e., high q , χ , and $\theta \approx 150^\circ$), inline with our expectations described in Sec. II A. We also see fewer predicted violations at lower SNR. This makes sense,

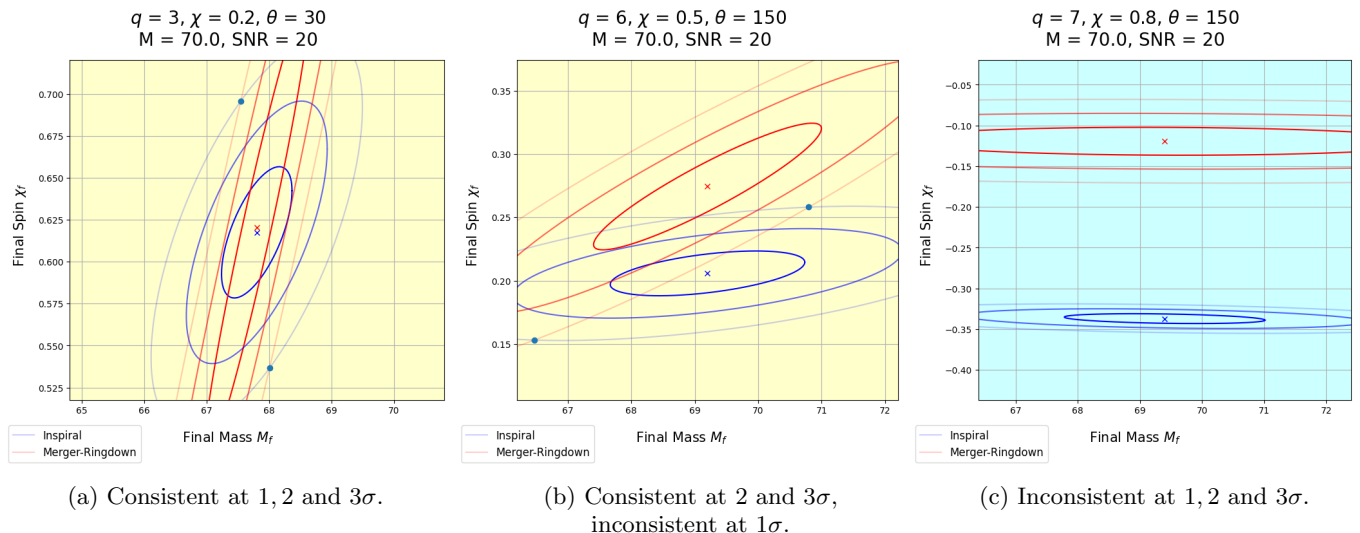


Figure 3: Fisher formalism IMR-consistency analysis results for 1, 2 and 3σ confidence levels are shown in the figure. The input inspiral parameters are displayed at the top of each figure. The recovered parameters (M_f, χ_f) from the inspiral and merger-ringdown of the waveform are marked with ‘x’ points, and the error ellipses, calculated using the Fisher matrix method, are plotted centered on these points. Consistency between the inspiral and merger-ringdown spin estimates at a specific confidence level occurs if the the error ellipses generated by the two sections overlap.

Results demonstrating consistency at 3σ level are highlighted with a yellow background, while inconsistency is denoted by a blue background.

as we expect our error ellipses to scale with $1/\sqrt{\text{SNR}}$ [73]. If our error ellipses are larger, systematic bias effects are less pronounced. This also means that as SNR increases, we see violations across a larger region of parameter space, as for larger SNRs our error ellipses should be smaller.

Fig. 3 illustrates the results of our analysis for three specific cases, at different points from widely separated regions in parameter space to demonstrate the observed parameter space trend. We investigate at confidence levels of 1σ , 2σ , and 3σ , plotting $x\sigma$ error ellipses centered around the values estimated in Section III A. In a standard IMR-consistency test, non-overlapping $x\sigma$ error ellipses indicates a potential deviation from GR at $x\sigma$ level. In our analysis here, such non-overlap would constitute an inconsistency in the model for the given input parameters, warranting caution in these specific parameter space regions.

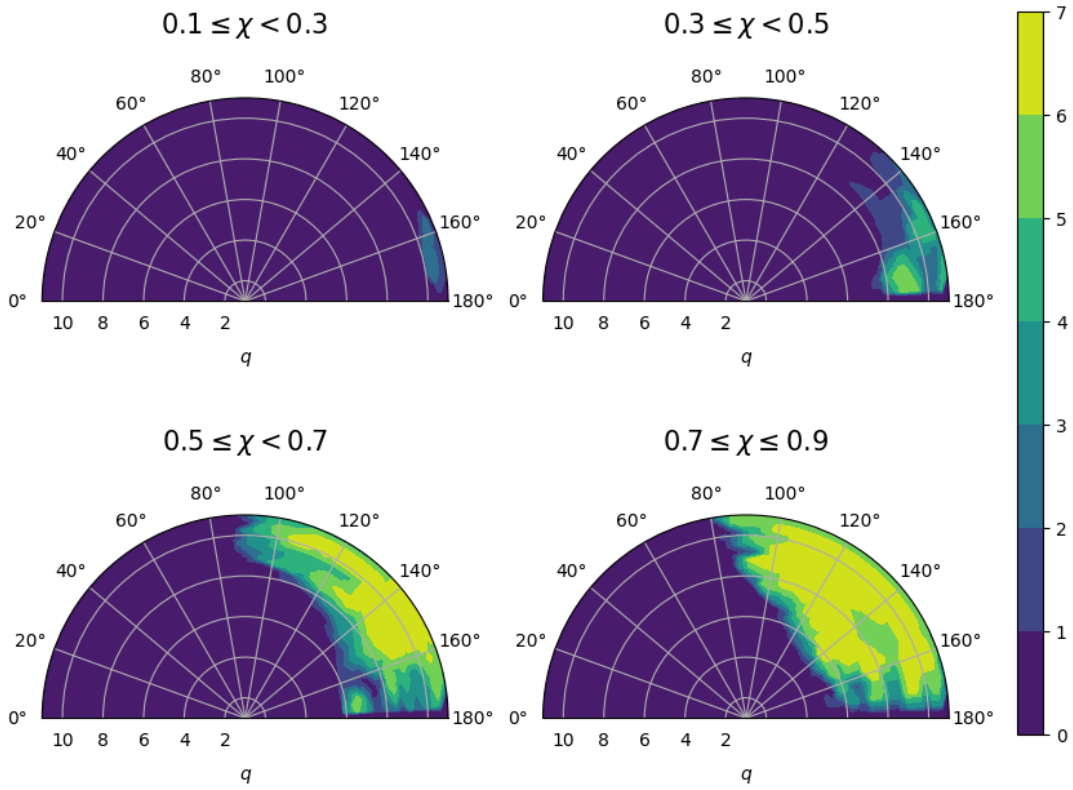
Our results follow our expectations as outlined in Sec. II A. The leftmost figure shows results for a weakly precessing system with low values of (q, χ, θ) , where even the 1σ error ellipses overlap. Therefore, the model is consistent for this system. However, this is not the case for the other two configurations. The middle figure shows a system with $(q = 6, \chi = 0.5, \theta = 150^\circ)$. Here, the model is consistent at 2σ and 3σ level, but is inconsistent at 1σ . The rightmost figure shows the most strongly precessing system with $(q = 7, \chi = 0.8, \theta = 150^\circ)$. Here we see that the model predicts a violation at all σ levels. We can clearly see that as we move towards more highly precessing systems, the deviation between the final

spin estimate calculated using the two methods increases from $\mathcal{O}(10^{-3})$ (left hand panel) to $\mathcal{O}(10^{-1})$ (right hand panel). Therefore, although the fractional uncertainty estimate remains constant, the error ellipses are much more strongly separated in the case of a highly precessing system.

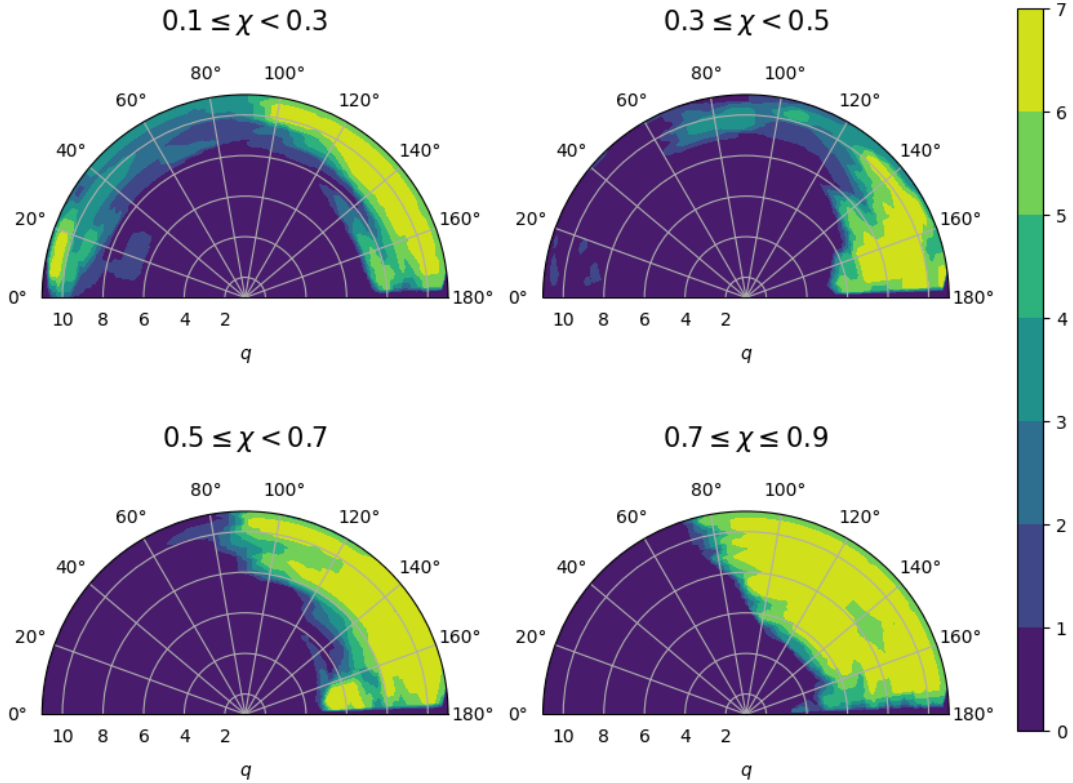
Having examined a few specific cases, we now aim to systematically explore trends across parameter space. To this end, we perform a similar analysis to the one described above for $28 \times 28 \times 28 = 21,952$ points in parameter space. This analysis is conducted for a given total mass, SNR, and σ level. Although most of the violation points appear in the region where we expect them, we still observe some scattered throughout the rest of parameter space. To identify general trends, we apply a noise reduction technique to our data.

The results, as seen in Fig. 4, show violations in the high (q, χ, θ) regions of parameter space as expected. We see that as each of the parameters gets closer to the region of expected violation (high q and χ , θ approaching 150°), there is an increased clustering of violation points. Comparing Fig. 4a to Fig. 4b, we see that an increase in SNR correlates with a broader violation region.

We also performed this analysis for varying values of SNR, and at 1σ , 2σ , and 3σ . In general, the region of parameter space in which we see inconsistencies at a given σ increases for higher SNR. This result aligns with the expectation that increased uncertainty in our estimates, reflected by larger error ellipses, facilitates overlooking systematic biases. This also means that as our detectors become more sensitive, and we begin detecting highly



(a) IMR-consistency test violation points at 3σ , for systems with total mass $M = 70M_{\odot}$ and SNR = 20.



(b) IMR-consistency test violation points at 3σ , for systems with total mass $M = 70M_{\odot}$ and SNR = 50.

Figure 4: These plots illustrate the results of an IMR-consistency test analysis conducted across parameter space, for $28 \times 28 \times 28$ points. The results are split into four bins depending on the χ input value. The radial axis shows q , and the angular axis shows θ . In each χ bin, there are 7 possible χ points for each (q, θ) . The plots here show the number of violations across χ for each (q, θ) , in each bin, with the colour bar showing this number. We clearly see more violations for higher χ , and clustered around high q and θ . From the difference between plots (a) and (b), we see the effect that SNR has on this analysis.

precessing systems, this bias will be more significant.

IV. PARAMETER ESTIMATION

In this section, we wish to investigate the effect of the systematic bias due to the mismodelling of ringdown frequency on a complete parameter estimation analysis. We seek to understand how parameter estimation may be biased, in particular for high mass systems where the merger and ringdown lie in the most sensitive part of the detector. We inject waveforms and run Bayesian analysis using parameter estimation pipelines. Attempts were also made to conduct IMR-consistency test injections and parameter estimation; however, the parameter recovery for the ringdown section was too poor to isolate the effects of the systematic bias under investigation.

Our injected waveform uses a modified version of IMRP_{HENOM}XPHM. IMRP_{HENOM}XPHM is built using the aligned-spin model IMRP_{HENOM}XHM [24] in the co-precessing frame, before applying a twisting-up procedure. In our analysis here, we use a version of IMRP_{HENOM}XPHM with an altered co-precessing frame model called XHM-CP [27, 29]. This modified version of the aligned spin model IMRP_{HENOM}XHM was used as part of the co-precessing frame model for the new precessing waveform model IMRP_{HENOM}XO4a [29]. XHM-CP shifts the QNM frequencies in the co-precessing frame, such that they are then accurately modelled in the inertial frame. Other small improvements are included in XHM-CP to improve the accuracy of the model as a whole, mainly affecting the late inspiral-merger section of the model. The dominant change in this co-precessing frame model is the ringdown frequencies, and we thus expect our analysis here to reflect specifically the effect of mismodelling the co-precessing ringdown frequency. We call this version of IMRP_{HENOM}XPHM with the correct shifted QNM frequency XPHM-FS.

We inject waveforms using XPHM-FS, and then recover parameters using both XPHM-FS and XPHM, models—the latter still containing the mismodelled QNM frequencies. This parameter estimation is done on the full waveform, instead of a waveform split in two sections for an IMR-consistency test. Given the computational intensity of this analysis, it was conducted on a limited number of configurations. In total, we performed injections for eight sets of intrinsic parameters (q, χ, θ) , which were $\{(3, 0.2, 0^\circ), (3, 0.2, 60^\circ), (3, 0.2, 90^\circ), (3, 0.8, 90^\circ), (3, 0.8, 150^\circ), (8, 0.2, 60^\circ), (8, 0.8, 90^\circ), (8, 0.8, 150^\circ)\}$. For each of these parameters, we injected at total mass $70M_\odot$ and $100M_\odot$, and at SNRs 20 and 60. The full set of parameters used for the injection analysis shown in Fig. 5 is listed in Table I. The extrinsic parameters were constant for all configurations considered. For each of the injections, we considered a three detector network, LIGO Livingston, LIGO Hanford, and VIRGO. The corresponding advanced design sensitivity curve were used for each of these detectors [8–10].

The choice of total mass $70M_\odot$ means that the ringdown frequency of the waveform is close to 100 - 200 Hz, which is the most sensitive frequency band of the LIGO and VIRGO detectors [8–10]. For systems with a high total mass such as this, the ringdown section of the signal will dominate our data, and mismodelling in the ringdown section will then greatly affect our parameter estimation results.

Right ascension, declination, polarisation, and inclination were chosen to ensure that the power in the plus and cross polarisations is approximately equal, enhancing the measurability of precession. Specifically, our goal was to achieve a ratio close to 1, expressed as $\sqrt{\sum_d F_{+,d}^2 / \sum_d F_{\times,d}^2} \sim 1$, where d represents the detectors. The choice of inclination was also optimised to maximise the observability of precession [87, 88].

We then performed Bayesian inference via the Bilby parameter estimation software package [89, 90] employing the Dynesty nested sampler [91] with 1000 live points and broad, uninformative priors. The injections and parameter estimation were performed using tools from yumeng.xu/GWUtils [92] on the LIGO Hawk computing cluster. The results were then processed and visualized using the pesummary package [93], which also facilitated the conversion of inspiral parameter posteriors to remnant parameter posteriors.

Total Mass $M[M_\odot]$	70
Mass Ratio q	3.0
Spin Magnitude χ	0.8
Spin Inclination $\theta[^\circ]$	150
Right ascension α	0.254
Declination δ	-0.111
Polarisation Ψ	4.697
Inclination ι	0.6

Table I: Parameters of the injection for results shown in Fig. 5.

Our injections range from aligned-spin to highly precessing systems, and in particular systems with high spin magnitudes and $\theta \approx 150^\circ$. The results of our parameter estimation are largely aligned with our expectations. For the $q = 3$ systems, the aligned spin and close to aligned spin systems showed good agreement between remnant parameter posteriors estimated from inspiral and merger-ringdown. As the spin magnitude χ and angle θ increase, discrepancies in the estimated remnant parameters become more pronounced, reaching a peak in the system outlined in Table I. Systems with $q = 8$ also exhibited some discrepancies in the estimated remnant parameters, exceeding the anticipated levels due to inaccuracies in modelling the ringdown frequency. This suggests that other systematics, such as the mismodelling of precessional dynamics through merger and ringdown, dominate the results such that we are unable to identify the impact of a given source of systematic bias.

The findings of the analysis for the system described in

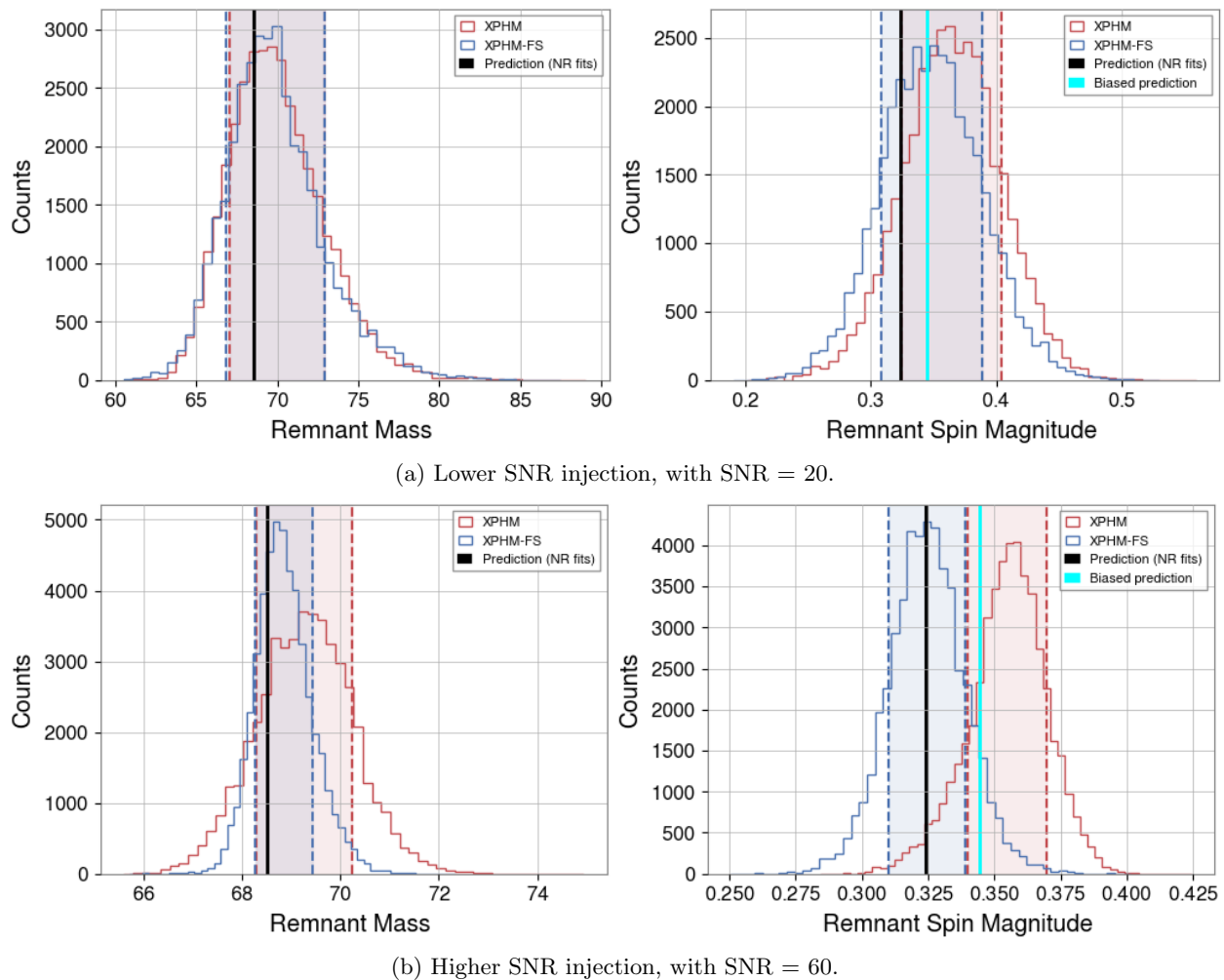


Figure 5: Injection and parameter estimation study results at two different SNR values, for a system with $M = 70$, $q = 3$, $\chi = 0.8$ and $\theta = 150^\circ$. For both figures, the remnant mass is in units $[M_\odot]$. The predicted values are remnant parameters estimated from the two sections of the waveform, following analysis detailed in Sec. III A 1 and Sec. III A 2. The shaded regions show the 1σ confidence regions.

Table I are illustrated in Fig. 5, which shows parameter estimation results at SNRs of 20 and 60. The remnant mass posteriors for the two models agree at 1σ , further justifying our assumption that $M_f^{\text{insp}} = M_f^{\text{merg}}$. In this figure, the ‘Prediction (NR fits)’ line on the right correspond to the true injected value calculated from NR fits, while the ‘Biased prediction’ line corresponds to the wrong value that we expect the mismodelling of the ringdown frequency to give. At lower SNR, shown in Fig. 5a, we see that both models recover the true injected value to 1σ confidence. However, at a higher SNR of 60, depicted in Fig. 5b, the disparity between the two posteriors for the final spin becomes evident, with XPHM failing to accurately recover the true injected value within the 1σ range, leaning instead towards the biased predicted value. This highlights the systematic bias that will occur when performing parameter estimation with any waveform model with this mismodelling of the ringdown fre-

quency.

The majority of events detected thus far have shown no clear evidence of precession and are at lower SNRs, belonging to the region of parameter space where we do not see biases from mismodelling this ringdown frequency. In the future, we expect the effects of this mismodelling to be relevant as detectors become increasingly sensitive and we begin to see unambiguously precessing signals.

V. CONCLUSION

With the ongoing observing run of the LVK [94], we anticipate the detection of a significant number of GW events with higher SNRs than previously seen. Additionally, we expect to observe signals from systems with considerable precession. It is crucial to pinpoint the limitations of our current waveform models to properly in-

terpret this influx of data.

In this work, we explored a source of systematic bias stemming from the inaccurate calculation of the co-precessing frame QNM frequency ω_{22}^{CP} , which results in an erroneous final inertial frame QNM frequency ω_{22}^{I} , and consequently, incorrect phenomenology in the post-merger waveform. We considered IMRPHENOMXPHM, a highly computationally efficient waveform model currently being used for data analysis. We identified the regions of the parameter space where this bias is strongest: namely where (q, χ) are high, and $\theta \sim 150^\circ$. Though the exact points of parameter space where this mismodelling is relevant is waveform model dependent, we expect the general picture to be model independent.

We examined the bias in the context of the IMR-consistency test by using the Fisher matrix formalism, checking whether the predicted remnant spin χ_f from the waveform model itself was consistent between inspiral and merger-ringdown portions of the waveform. The computational efficiency of the Fisher matrix formalism enabled us to run this analysis across the entire parameter space. Our results demonstrated discrepancies between the inspiral and merger-ringdown sections of the model, for high values of (q, χ) , and $\theta \sim 150^\circ$ as expected. We found that the discrepancies are greater at larger SNR.

Additionally, we found that employing models that do not correctly account for the effect of precession in the ringdown frequency can lead to biased parameter estimation results, which is particularly significant at higher SNRs.

In conclusion, our results have shown how failing to correctly account for all physical effects can lead to waveform systematics that negatively impact both parameter estimation and tests of GR. Here we have focused on precession effects in the merger-ringdown portion of the signal. The majority of currently available waveform models for use in analysis do not completely model precession through merger and ringdown accurately. In addition, we are yet to have full GR-informed models that account for both precession and eccentricity, which will add further biases in parameter estimation.

VI. ACKNOWLEDGEMENTS

The authors of this paper would like to thank Shubhanshu Tiwari, Yumeng Xu, Philippe Jetzer, Héctor Estellés, Peter James Nee, Nihar Gupte, Raj Patil, and Elisa Maggio for useful discussions. We would also like to thank Krishnendu N V for her useful comments on the manuscript.

EH was supported in part by Swiss National Science Foundation (SNSF) grant IZCOZ0-189876 and by UZH Postdoc Grant (Forschungskredit) FK-22-115. EH was also supported in part by the Universitat de les Illes Balears (UIB); the Spanish Agencia Estatal de Investigación grants PID2022-138626NB-I00, PID2019-

106416GB-I00, RED2022-134204-E, RED2022-134411-T, funded by MCIN/AEI/10.13039/501100011033; the MCIN with funding from the European Union NextGenerationEU/PRTR (PRTR-C17.11); Comunitat Autònoma de les Illes Balears through the Direcció General de Recerca, Innovació i Transformació Digital with funds from the Tourist Stay Tax Law (PDR2020/11 - ITS2017-006), the Conselleria d’Economia, Hisenda i Innovació grant numbers SINCO2022/18146 and SINCO2022/6719, co-financed by the European Union and FEDER Operational Program 2021-2027 of the Balearic Islands; the “ERDF A way of making Europe”.

The authors are grateful for computational resources provided by the Cardiff University and supported by STFC grants ST/I006285/1 and ST/V005618/1.

- [1] B. P. Abbott *et al.* (LIGO Scientific Collaboration and Virgo Collaboration), GWTC-1: A Gravitational-Wave Transient Catalog of Compact Binary Mergers Observed by LIGO and Virgo during the First and Second Observing Runs, *Phys. Rev. X* **9**, 031040 (2019).
- [2] R. Abbott *et al.* (LIGO Scientific, VIRGO), GWTC-2.1: Deep Extended Catalog of Compact Binary Coalescences Observed by LIGO and Virgo During the First Half of the Third Observing Run, *Phys. Rev. D* (2021), [arXiv:2108.01045 \[gr-qc\]](#).
- [3] R. Abbott *et al.* (LIGO Scientific, Virgo), GWTC-2: Compact Binary Coalescences Observed by LIGO and Virgo During the First Half of the Third Observing Run, *Phys. Rev. X* **11**, 021053 (2021), [arXiv:2010.14527 \[gr-qc\]](#).
- [4] R. Abbott *et al.* (LIGO Scientific, VIRGO, KAGRA), GWTC-3: Compact Binary Coalescences Observed by LIGO and Virgo during the Second Part of the Third Observing Run, *Physical Review X* **13**, 10.1103/physrevx.13.041039 (2023).
- [5] A. Gupta *et al.*, Possible Causes of False General Relativity Violations in Gravitational Wave Observations, (2024), [arXiv:2405.02197 \[gr-qc\]](#).
- [6] A. Dhani, S. Völkel, A. Buonanno, H. Estelles, J. Gair, H. P. Pfeiffer, L. Pompili, and A. Toubiana, Systematic Biases in Estimating the Properties of Black Holes Due to Inaccurate Gravitational-Wave Models (2024), [arXiv:2404.05811v \[gr-qc\]](#).
- [7] Q. Hu and J. Veitch, Assessing the model waveform accuracy of gravitational waves, *Phys. Rev. D* **106**, 044042 (2022), [arXiv:2205.08448 \[gr-qc\]](#).
- [8] B. P. Abbott *et al.* (KAGRA, LIGO Scientific, Virgo, VIRGO), Prospects for observing and localizing gravitational-wave transients with Advanced LIGO, Advanced Virgo and KAGRA, *Living Rev. Rel.* **21**, 3 (2018), [arXiv:1304.0670 \[gr-qc\]](#).
- [9] J. Aasi *et al.* (LIGO Scientific), Advanced LIGO, *Class. Quant. Grav.* **32**, 074001 (2015), [arXiv:1411.4547 \[gr-qc\]](#).
- [10] F. Acernese *et al.* (VIRGO), Advanced Virgo: a second-generation interferometric gravitational wave detector, *Class. Quant. Grav.* **32**, 024001 (2015), [arXiv:1408.3978 \[gr-qc\]](#).
- [11] Y. Aso, Y. Michimura, K. Somiya, M. Ando, O. Miyakawa, T. Sekiguchi, D. Tatsumi, and H. Yamamoto (The KAGRA Collaboration), Interferometer design of the KAGRA gravitational wave detector, *Phys. Rev. D* **88**, 043007 (2013).
- [12] D. Reitze *et al.*, Cosmic Explorer: The U.S. Contribution to Gravitational-Wave Astronomy beyond LIGO, *Bull. Am. Astron. Soc.* **51**, 035 (2019), [arXiv:1907.04833 \[astro-ph.IM\]](#).
- [13] M. Evans *et al.*, A Horizon Study for Cosmic Explorer: Science, Observatories, and Community (2021), [arXiv:2109.09882 \[astro-ph.IM\]](#).
- [14] M. Punturo *et al.*, The einstein telescope: a third-generation gravitational wave observatory, *Classical and Quantum Gravity* **27**, 194002 (2010).
- [15] P. Amaro-Seoane *et al.*, Laser interferometer space antenna (2017), [arXiv:1702.00786 \[astro-ph.IM\]](#).
- [16] M. Hannam, P. Schmidt, A. Bohé, L. Haegel, S. Husa, F. Ohme, G. Pratten, and M. Pürrer, Simple Model of Complete Precessing Black-Hole-Binary Gravitational Waveforms, *Phys. Rev. Lett.* **113**, 151101 (2014), [arXiv:1308.3271 \[gr-qc\]](#).
- [17] S. Husa, S. Khan, M. Hannam, M. Pürrer, F. Ohme, X. Jiménez Forteza, and A. Bohé, Frequency-domain gravitational waves from nonprecessing black-hole binaries. I. New numerical waveforms and anatomy of the signal, *Phys. Rev. D* **93**, 044006 (2016), [arXiv:1508.07250 \[gr-qc\]](#).
- [18] S. Khan, S. Husa, M. Hannam, F. Ohme, M. Pürrer, X. Jiménez Forteza, and A. Bohé, Frequency-domain gravitational waves from nonprecessing black-hole binaries. II. A phenomenological model for the advanced detector era, *Phys. Rev. D* **93**, 044007 (2016), [arXiv:1508.07253 \[gr-qc\]](#).
- [19] L. London, S. Khan, E. Fauchon-Jones, C. García, M. Hannam, S. Husa, X. Jiménez-Forteza, C. Kalaghatgi, F. Ohme, and F. Pannarale, First higher-multipole model of gravitational waves from spinning and coalescing black-hole binaries, *Phys. Rev. Lett.* **120**, 161102 (2018), [arXiv:1708.00404 \[gr-qc\]](#).
- [20] S. Khan, K. Chatziioannou, M. Hannam, and F. Ohme, Phenomenological model for the gravitational-wave signal from precessing binary black holes with two-spin effects, *Phys. Rev. D* **100**, 024059 (2019), [arXiv:1809.10113 \[gr-qc\]](#).
- [21] S. Khan, F. Ohme, K. Chatziioannou, and M. Hannam, Including higher order multipoles in gravitational-wave models for precessing binary black holes, *Phys. Rev. D* **101**, 024056 (2020), [arXiv:1911.06050 \[gr-qc\]](#).
- [22] G. Pratten, S. Husa, C. Garcia-Quiros, M. Colleoni, A. Ramos-Buades, H. Estelles, and R. Jaume, Setting the cornerstone for a family of models for gravitational waves from compact binaries: The dominant harmonic for nonprecessing quasicircular black holes, *Phys. Rev. D* **102**, 064001 (2020), [arXiv:2001.11412 \[gr-qc\]](#).
- [23] G. Pratten *et al.*, Computationally efficient models for the dominant and subdominant harmonic modes of precessing binary black holes, *Phys. Rev. D* **103**, 104056 (2021), [arXiv:2004.06503 \[gr-qc\]](#).
- [24] C. García-Quirós, M. Colleoni, S. Husa, H. Estellés, G. Pratten, A. Ramos-Buades, M. Mateu-Lucena, and R. Jaume, Multimode frequency-domain model for the gravitational wave signal from nonprecessing black-hole binaries, *Phys. Rev. D* **102**, 064002 (2020), [arXiv:2001.10914 \[gr-qc\]](#).
- [25] H. Estellés, A. Ramos-Buades, S. Husa, C. García-Quirós, M. Colleoni, L. Haegel, and R. Jaume, Phenomenological time domain model for dominant quadrupole gravitational wave signal of coalescing binary black holes, *Phys. Rev. D* **103**, 124060 (2021), [arXiv:2004.08302 \[gr-qc\]](#).
- [26] H. Estellés, S. Husa, M. Colleoni, D. Keitel, M. Mateu-Lucena, C. García-Quirós, A. Ramos-Buades, and A. Borchers, Time-domain phenomenological model of gravitational-wave subdominant harmonics for quasicircular nonprecessing binary black hole coalescences, *Phys. Rev. D* **105**, 084039 (2022), [arXiv:2012.11923 \[gr-qc\]](#).
- [27] E. Hamilton, L. London, J. E. Thompson, E. Fauchon-Jones, M. Hannam, C. Kalaghatgi, S. Khan, F. Pannarale, and A. Vano-Vinuales, Model of gravitational

- waves from precessing black-hole binaries through merger and ringdown, *Phys. Rev. D* **104**, 124027 (2021), [arXiv:2107.08876 \[gr-qc\]](#).
- [28] H. Estellés, M. Colleoni, C. García-Quirós, S. Husa, D. Keitel, M. Mateu-Lucena, M. d. L. Planas, and A. Ramos-Buades, New twists in compact binary waveform modeling: A fast time-domain model for precession, *Phys. Rev. D* **105**, 084040 (2022), [arXiv:2105.05872 \[gr-qc\]](#).
- [29] J. E. Thompson, E. Hamilton, L. London, S. Ghosh, P. Kolitsidou, C. Hoy, and M. Hannam, PhenomXO4a: a phenomenological gravitational-wave model for precessing black-hole binaries with higher multipoles and asymmetries, *Phys. Rev. D* **109**, 063012 (2024), [arXiv:2312.10025 \[gr-qc\]](#).
- [30] A. Taracchini, Y. Pan, A. Buonanno, E. Barausse, M. Boyle, T. Chu, G. Lovelace, H. P. Pfeiffer, and M. A. Scheel, Prototype effective-one-body model for nonprecessing spinning inspiral-merger-ringdown waveforms, *Phys. Rev. D* **86**, 024011 (2012), [arXiv:1202.0790 \[gr-qc\]](#).
- [31] A. Taracchini *et al.*, Effective-one-body model for black-hole binaries with generic mass ratios and spins, *Phys. Rev. D* **89**, 061502 (2014), [arXiv:1311.2544 \[gr-qc\]](#).
- [32] Y. Pan, A. Buonanno, A. Taracchini, L. E. Kidder, A. H. Mroué, H. P. Pfeiffer, M. A. Scheel, and B. Szilágyi, Inspiral-merger-ringdown waveforms of spinning, precessing black-hole binaries in the effective-one-body formalism, *Phys. Rev. D* **89**, 084006 (2014), [arXiv:1307.6232 \[gr-qc\]](#).
- [33] A. Bohé *et al.*, Improved effective-one-body model of spinning, nonprecessing binary black holes for the era of gravitational-wave astrophysics with advanced detectors, *Phys. Rev. D* **95**, 044028 (2017), [arXiv:1611.03703 \[gr-qc\]](#).
- [34] R. Cotesta, A. Buonanno, A. Bohé, A. Taracchini, I. Hinder, and S. Ossokine, Enriching the Symphony of Gravitational Waves from Binary Black Holes by Tuning Higher Harmonics, *Phys. Rev. D* **98**, 084028 (2018), [arXiv:1803.10701 \[gr-qc\]](#).
- [35] S. Ossokine *et al.*, Multipolar Effective-One-Body Waveforms for Precessing Binary Black Holes: Construction and Validation, *Phys. Rev. D* **102**, 044055 (2020), [arXiv:2004.09442 \[gr-qc\]](#).
- [36] L. Pompili *et al.*, Laying the foundation of the effective-one-body waveform models SEOBNRv5: Improved accuracy and efficiency for spinning nonprecessing binary black holes, *Phys. Rev. D* **108**, 124035 (2023), [arXiv:2303.18039 \[gr-qc\]](#).
- [37] A. Ramos-Buades, A. Buonanno, H. Estellés, M. Khalil, D. P. Mihaylov, S. Ossokine, L. Pompili, and M. Shiferaw, Next generation of accurate and efficient multipolar precessing-spin effective-one-body waveforms for binary black holes, *Phys. Rev. D* **108**, 124037 (2023), [arXiv:2303.18046 \[gr-qc\]](#).
- [38] J. Blackman, S. E. Field, C. R. Galley, B. Szilágyi, M. A. Scheel, M. Tiglio, and D. A. Hemberger, Fast and Accurate Prediction of Numerical Relativity Waveforms from Binary Black Hole Coalescences Using Surrogate Models, *Phys. Rev. Lett.* **115**, 121102 (2015), [arXiv:1502.07758 \[gr-qc\]](#).
- [39] J. Blackman, S. E. Field, M. A. Scheel, C. R. Galley, D. A. Hemberger, P. Schmidt, and R. Smith, A Surrogate Model of Gravitational Waveforms from Numerical Relativity Simulations of Precessing Binary Black Hole Mergers, *Phys. Rev. D* **95**, 104023 (2017), [arXiv:1701.00550 \[gr-qc\]](#).
- [40] J. Blackman, S. E. Field, M. A. Scheel, C. R. Galley, C. D. Ott, M. Boyle, L. E. Kidder, H. P. Pfeiffer, and B. Szilágyi, Numerical relativity waveform surrogate model for generically precessing binary black hole mergers, *Phys. Rev. D* **96**, 024058 (2017), [arXiv:1705.07089 \[gr-qc\]](#).
- [41] V. Varma, S. E. Field, M. A. Scheel, J. Blackman, L. E. Kidder, and H. P. Pfeiffer, Surrogate model of hybridized numerical relativity binary black hole waveforms, *Phys. Rev. D* **99**, 064045 (2019), [arXiv:1812.07865 \[gr-qc\]](#).
- [42] V. Varma, S. E. Field, M. A. Scheel, J. Blackman, D. Gerosa, L. C. Stein, L. E. Kidder, and H. P. Pfeiffer, Surrogate models for precessing binary black hole simulations with unequal masses, *Phys. Rev. Research* **1**, 033015 (2019), [arXiv:1905.09300 \[gr-qc\]](#).
- [43] D. Williams, I. S. Heng, J. Gair, J. A. Clark, and B. Khamesra, Precessing numerical relativity waveform surrogate model for binary black holes: A Gaussian process regression approach, *Phys. Rev. D* **101**, 063011 (2020), [arXiv:1903.09204 \[gr-qc\]](#).
- [44] N. E. M. Rifat, S. E. Field, G. Khanna, and V. Varma, Surrogate model for gravitational wave signals from comparable and large-mass-ratio black hole binaries, *Phys. Rev. D* **101**, 081502 (2020), [arXiv:1910.10473 \[gr-qc\]](#).
- [45] T. Islam, V. Varma, J. Lodman, S. E. Field, G. Khanna, M. A. Scheel, H. P. Pfeiffer, D. Gerosa, and L. E. Kidder, Eccentric binary black hole surrogate models for the gravitational waveform and remnant properties: comparable mass, nonspinning case, *Phys. Rev. D* **103**, 064022 (2021), [arXiv:2101.11798 \[gr-qc\]](#).
- [46] T. Islam, S. E. Field, S. A. Hughes, G. Khanna, V. Varma, M. Giesler, M. A. Scheel, L. E. Kidder, and H. P. Pfeiffer, Surrogate model for gravitational wave signals from nonspinning, comparable-to large-mass-ratio black hole binaries built on black hole perturbation theory waveforms calibrated to numerical relativity, *Phys. Rev. D* **106**, 104025 (2022), [arXiv:2204.01972 \[gr-qc\]](#).
- [47] D. Gerosa, E. Berti, R. O’Shaughnessy, K. Belczynski, M. Kesden, D. Wysocki, and W. Gladysz, Spin orientations of merging black holes formed from the evolution of stellar binaries, *Phys. Rev. D* **98**, 084036 (2018), [arXiv:1808.02491 \[astro-ph.HE\]](#).
- [48] S. Kulkarni, N. K. Johnson-McDaniel, K. S. Phukon, N. V. Krishnendu, and A. Gupta, Inferring spin tilts of binary black holes at formation with plus-era gravitational wave detectors, *Phys. Rev. D* **109**, 043002 (2024), [arXiv:2308.05098 \[astro-ph.HE\]](#).
- [49] T. A. Apostolatos, C. Cutler, G. J. Sussman, and K. S. Thorne, Spin induced orbital precession and its modulation of the gravitational wave forms from merging binaries, *Phys. Rev. D* **49**, 6274 (1994).
- [50] V. Varma, L. C. Stein, and D. Gerosa, The binary black hole explorer: on-the-fly visualizations of precessing binary black holes, *Class. Quant. Grav.* **36**, 095007 (2019), [arXiv:1811.06552 \[astro-ph.HE\]](#).
- [51] M. Hannam, Modelling gravitational waves from precessing black-hole binaries: Progress, challenges and prospects, *Gen. Rel. Grav.* **46**, 1767 (2014), [arXiv:1312.3641 \[gr-qc\]](#).
- [52] A. Buonanno, Y.-b. Chen, and M. Vallisneri, Detecting gravitational waves from precessing binaries of spin-

- ning compact objects: Adiabatic limit, *Phys. Rev. D* **67**, 104025 (2003), [Erratum: *Phys.Rev.D* 74, 029904 (2006)], [arXiv:gr-qc/0211087](#).
- [53] P. Schmidt, M. Hannam, S. Husa, and P. Ajith, Tracking the precession of compact binaries from their gravitational-wave signal, *Phys. Rev. D* **84**, 024046 (2011), [arXiv:1012.2879 \[gr-qc\]](#).
- [54] P. Schmidt, M. Hannam, and S. Husa, Towards models of gravitational waveforms from generic binaries: A simple approximate mapping between precessing and non-precessing inspiral signals, *Phys. Rev. D* **86**, 104063 (2012), [arXiv:1207.3088 \[gr-qc\]](#).
- [55] E. W. Leaver, An analytic representation for the quasi normal modes of kerr black holes, *Proc. Roy. Soc. Lond. A* **402**, 285 (1985).
- [56] E. Berti and A. Klein, Mixing of spherical and spheroidal modes in perturbed kerr black holes, *Phys. Rev. D* **90**, 064012 (2014), [arXiv:1408.1860 \[gr-qc\]](#).
- [57] R. O’Shaughnessy, L. London, J. Healy, and D. Shoemaker, Precession during merger: Strong polarization changes are observationally accessible features of strong-field gravity during binary black hole merger, *Phys. Rev. D* **87**, 044038 (2013), [arXiv:1209.3712 \[gr-qc\]](#).
- [58] E. Hamilton, L. London, and M. Hannam, Ringdown frequencies in black holes formed from precessing black-hole binaries, *Phys. Rev. D* **107**, 104035 (2023), [arXiv:2301.06558 \[gr-qc\]](#).
- [59] H. Zhu *et al.*, Black Hole Spectroscopy for Precessing Binary Black Hole Coalescences, (2023), [arXiv:2312.08588 \[gr-qc\]](#).
- [60] A. Ghosh, N. K. Johnson-McDaniel, A. Ghosh, C. K. Mishra, P. Ajith, W. Del Pozzo, C. P. L. Berry, A. B. Nielsen, and L. London, Testing general relativity using gravitational wave signals from the inspiral, merger and ringdown of binary black holes, *Class. Quant. Grav.* **35**, 014002 (2018), [arXiv:1704.06784 \[gr-qc\]](#).
- [61] B. P. Abbott *et al.* (LIGO Scientific, Virgo), Tests of General Relativity with the Binary Black Hole Signals from the LIGO-Virgo Catalog GWTC-1, *Phys. Rev. D* **100**, 104036 (2019), [arXiv:1903.04467 \[gr-qc\]](#).
- [62] S. A. Hughes and K. Menou, Golden binaries for LISA: Robust probes of strong-field gravity, *Astrophys. J.* **623**, 689 (2005), [arXiv:astro-ph/0410148](#).
- [63] P. Ajith *et al.*, Inspiral-merger-ringdown waveforms for black-hole binaries with non-precessing spins, *Phys. Rev. Lett.* **106**, 241101 (2011), [arXiv:0909.2867 \[gr-qc\]](#).
- [64] L. Santamaria *et al.*, Matching post-Newtonian and numerical relativity waveforms: systematic errors and a new phenomenological model for non-precessing black hole binaries, *Phys. Rev. D* **82**, 064016 (2010), [arXiv:1005.3306 \[gr-qc\]](#).
- [65] P. Schmidt, F. Ohme, and M. Hannam, Towards models of gravitational waveforms from generic binaries II: Modelling precession effects with a single effective precession parameter, *Phys. Rev. D* **91**, 024043 (2015), [arXiv:1408.1810 \[gr-qc\]](#).
- [66] E. Berti, V. Cardoso, and A. O. Starinets, Quasinormal modes of black holes and black branes, *Class. Quant. Grav.* **26**, 163001 (2009), [arXiv:0905.2975 \[gr-qc\]](#).
- [67] L. T. London, Biorthogonal harmonics for the decomposition of gravitational radiation. I. Angular modes, completeness, and the introduction of adjoint-spheroidal harmonics, *Phys. Rev. D* **107**, 044056 (2023), [arXiv:2006.11449 \[gr-qc\]](#).
- [68] R. O’Shaughnessy, B. Vaishnav, J. Healy, Z. Meeks, and D. Shoemaker, Efficient asymptotic frame selection for binary black hole spacetimes using asymptotic radiation, *Phys. Rev. D* **84**, 124002 (2011), [arXiv:1109.5224 \[gr-qc\]](#).
- [69] R. Abbott *et al.* (LIGO Scientific, VIRGO, KAGRA), Tests of General Relativity with GWTC-3, (2021), [arXiv:2112.06861 \[gr-qc\]](#).
- [70] F. Hofmann, E. Barausse, and L. Rezzolla, The final spin from binary black holes in quasi-circular orbits, *Astrophys. J. Lett.* **825**, L19 (2016), [arXiv:1605.01938 \[gr-qc\]](#).
- [71] J. Centrella, J. G. Baker, B. J. Kelly, and J. R. van Meter, Black-hole binaries, gravitational waves, and numerical relativity, *Rev. Mod. Phys.* **82**, 3069 (2010), [arXiv:1010.5260 \[gr-qc\]](#).
- [72] M. Vallisneri, Use and abuse of the Fisher information matrix in the assessment of gravitational-wave parameter-estimation prospects, *Phys. Rev. D* **77**, 042001 (2008), [arXiv:gr-qc/0703086](#).
- [73] M. Maggiore, *Gravitational Waves. Vol. 1: Theory and Experiments* (Oxford University Press, 2007).
- [74] C. Cutler and E. E. Flanagan, Gravitational waves from merging compact binaries: How accurately can one extract the binary’s parameters from the inspiral wave form?, *Phys. Rev. D* **49**, 2658 (1994), [arXiv:gr-qc/9402014](#).
- [75] S. A. Bhat, P. Saini, M. Favata, and K. G. Arun, Systematic bias on the inspiral-merger-ringdown consistency test due to neglect of orbital eccentricity, *Phys. Rev. D* **107**, 024009 (2023), [arXiv:2207.13761 \[gr-qc\]](#).
- [76] A. Nitz, I. Harry, D. Brown, C. M. Biwer, J. Willis, T. D. Canton, C. Capano, T. Dent, L. Pekowsky, A. R. Williamson, S. De, M. Cabero, B. Machenschalk, D. Macleod, P. Kumar, F. Pannarale, S. Reyes, G. S. C. Davies, dfinstad, S. Kumar, M. Tápai, L. Singer, S. Khan, S. Fairhurst, A. Nielsen, S. Singh, T. Massinger, K. Chandra, shasvath, and veronica villa, [gwastro/pycbc: v2.0.5 release of pycbc](#) (2022).
- [77] J. M. Bardeen, W. H. Press, and S. A. Teukolsky, Rotating black holes: Locally nonrotating frames, energy extraction, and scalar synchrotron radiation, *Astrophys. J.* **178**, 347 (1972).
- [78] M. Favata, C. Kim, K. G. Arun, J. Kim, and H. W. Lee, Constraining the orbital eccentricity of inspiralling compact binary systems with Advanced LIGO, *Phys. Rev. D* **105**, 023003 (2022), [arXiv:2108.05861 \[gr-qc\]](#).
- [79] X. Jiménez-Forteza, D. Keitel, S. Husa, M. Hannam, S. Khan, and M. Pürrer, Hierarchical data-driven approach to fitting numerical relativity data for nonprecessing binary black holes with an application to final spin and radiated energy, *Phys. Rev. D* **95**, 064024 (2017), [arXiv:1611.00332 \[gr-qc\]](#).
- [80] L. London, E. Fauchon, and EZHamilton, [llondon6/positive](#) (2020).
- [81] N. K. Johnson-McDaniel, A. Gupta, P. Ajith, D. Keitel, O. Birnholtz, F. Ohme, and S. Husa, Determining the final spin of a binary black hole system including in-plane spins: Method and checks of accuracy, *LIGO Document T1600168-v6* (2016).
- [82] V. Varma, D. Gerosa, L. C. Stein, F. Hébert, and H. Zhang, High-accuracy mass, spin, and recoil predictions of generic black-hole merger remnants, *Phys. Rev. Lett.* **122**, 011101 (2019), [arXiv:1809.09125 \[gr-qc\]](#).
- [83] N. Siemonsen, J. Steinhoff, and J. Vines, Gravitational waves from spinning binary black holes at the leading

- post-Newtonian orders at all orders in spin, *Phys. Rev. D* **97**, 124046 (2018), [arXiv:1712.08603 \[gr-qc\]](#).
- [84] A. Bohé, M. Hannam, S. Husa, F. Ohme, M. Pürrer, and P. Schmidt, Phenompv2 - technical notes for the lal implementation, *LIGO Document T1500602-v4* (2016).
- [85] S. Khan and E. Fauchon, [gw-phenom](#) (2020).
- [86] K. Chatziioannou, A. Klein, N. Yunes, and N. Cornish, Constructing Gravitational Waves from Generic Spin-Precessing Compact Binary Inspirals, *Phys. Rev. D* **95**, 104004 (2017), [arXiv:1703.03967 \[gr-qc\]](#).
- [87] S. Fairhurst, R. Green, C. Hoy, M. Hannam, and A. Muir, Two-harmonic approximation for gravitational waveforms from precessing binaries, *Phys. Rev. D* **102**, 024055 (2020), [arXiv:1908.05707 \[gr-qc\]](#).
- [88] R. Green, C. Hoy, S. Fairhurst, M. Hannam, F. Panarale, and C. Thomas, Identifying when Precession can be Measured in Gravitational Waveforms, *Phys. Rev. D* **103**, 124023 (2021), [arXiv:2010.04131 \[gr-qc\]](#).
- [89] G. Ashton *et al.*, BILBY: A user-friendly Bayesian inference library for gravitational-wave astronomy, *Astrophys. J. Suppl.* **241**, 27 (2019), [arXiv:1811.02042 \[astro-ph.IM\]](#).
- [90] I. M. Romero-Shaw *et al.*, Bayesian inference for compact binary coalescences with bilby: validation and application to the first LIGO–Virgo gravitational-wave transient catalogue, *Monthly Notices of the Royal Astronomical Society* **499**, 3295 (2020), <https://academic.oup.com/mnras/article-pdf/499/3/3295/34052625/staa2850.pdf>.
- [91] J. S. Speagle, dynesty: a dynamic nested sampling package for estimating bayesian posteriors and evidences, *Monthly Notices of the Royal Astronomical Society* **493**, 3132–3158 (2020).
- [92] Y. Xu, [gw-utils](#) (2023).
- [93] C. Hoy and V. Raymond, PESummary: the code agnostic Parameter Estimation Summary page builder, *SoftwareX* **15**, 100765 (2021), [arXiv:2006.06639 \[astro-ph.IM\]](#).
- [94] L. Collaboration, Latest update on start of next observing run (o4) (2022).